Magnetic Fields from Superfast Rotating Astronomical Bodies

Saoussan Kallel-Jallouli

ORCID ID: 0000-0002-2873-698X

Université de Tunis El Manar, LR03ES04, Faculté des Sciences de Tunis, 2092, Tunis, Tunisia.

DOI: https://doi.org/10.51584/IJRIAS.2026.11013SP0008

Received: 04 February 2026; Accepted: 10 February 2026; Published: 19 February 2026

ABSTRACT

Magnetism has long been a driving force behind scientific discovery and technological innovation, shaping applications that now permeate everyday life. From magnetically levitated high-speed trains to minimally invasive medical microrobots navigating the human body, magnetic fields enable motion, control, and interaction across a remarkable range of scales and environments. Despite these advances, the role of magnetic fields in astrophysical systems remains incompletely understood and largely inferred rather than directly observed. To date, measurements of magnetic fields associated with astronomical bodies rely almost exclusively on indirect methods, notably the analysis of polarization changes in emitted or absorbed radiation. In this sense, our observational knowledge is derived from light, not from the magnetic field itself. Direct detection of astrophysical magnetic fields—particularly those that are weak and rapidly varying—has remained an outstanding challenge.

In this work, we propose a direct measurement technique capable of detecting faint magnetic fields produced by astronomical objects exhibiting rapid temporal variations. This method has been experimentally validated and demonstrates sensitivity beyond that of conventional indirect approaches. The proposed technology opens new possibilities for probing the influence of magnetic fields on stellar dynamics, evolution, and large-scale astrophysical processes. Direct magnetic field measurements would therefore represent a significant step toward a deeper and more comprehensive understanding of the physical universe.

Keywords: Magnetic fields; interferometry; wave phenomena; stellar magnetism

1. INTRODUCTION

Magnetic fields are widely recognized as a fundamental ingredient of stellar physics, yet their role in stellar structure and evolution remains incompletely understood. This limited understanding translates into significant uncertainties in stellar evolution models, particularly in relation to angular momentum transport, mass loss, and magnetic braking. Although magnetic fields are now believed to influence the evolution of many classes of stars, direct observational constraints remain scarce, and spectropolarimetric measurements are still available for only a limited sample of objects.

The measurement of stellar magnetic fields dates back to the pioneering work of Babcock (1947). Since then, observational techniques have relied almost exclusively on the polarization signatures produced by the Zeeman effect in spectral lines emitted by atoms embedded in magnetic fields (Hubrig et al. 2020a). Magnetic fields modify atomic energy levels, thereby affecting the polarization state of the emitted radiation. Consequently, all established methods infer the presence and strength of magnetic fields indirectly, through measurements of polarized photons rather than through direct detection of the field itself.

In practice, stellar magnetic field determinations are commonly expressed in terms of the mean longitudinal magnetic field, $\langle B_z \rangle$, corresponding to the line-of-sight component of the magnetic field and derived from light circular polarization measurements (Hubrig et al., 2020b). Early surveys, such as those conducted by Babcock, were further constrained by stellar rotational velocities, typically restricting targets to stars with projected

rotational speeds below 20–30 km s^{-1} (Lundin, 2010). As a result, observational biases and geometric limitations remain intrinsic to current magnetic field diagnostics.

The simplest and most widely adopted model for stellar magnetic field geometry is that of an oblique dipole rotator, in which the magnetic dipole axis is inclined with respect to the stellar rotation axis. Within this framework, observations generally allow only a lower limit to be placed on the dipolar field strength, commonly expressed as (Babcock, 1958):

$$B_d \geq |\langle B_z \rangle_{max}| \qquad (1.1)$$

The absence of direct magnetic field measurements thus represents a major limitation for advancing stellar evolution theories. A technique capable of directly detecting magnetic fields from astronomical bodies would be of exceptional value, offering new constraints on magnetic field strength, geometry, and temporal variability.

In this work, we explore the conditions under which direct measurements of magnetic fields from astronomical bodies may be possible. To this end, Section 2 reviews relevant classical concepts of magnetism and electromagnetic induction. Section 3 focuses on dipole magnets, associated magnetic waveforms, and field polarization, while Section 4 extends the analysis to quadrupolar configurations. Common magnetic field sensors are presented in Section 5, followed by a discussion in Section 6 on how such sensors may be improved and adapted for astronomical applications. Finally, Section 7 presents the discussion and interpretation of the results.

2. ELECTROMAGNETIC INDUCTION

Magnetic fields exert a fundamental influence on the motion of charged particles by altering their trajectories and inducing acceleration. A charged particle of electric charge q, moving with velocity $\boldsymbol{v}$ in a magnetic field

$\boldsymbol{B}$, experiences the Lorentz force $\boldsymbol{F}_L$, given by

$$\boldsymbol{F}_L = q\boldsymbol{v} \times \boldsymbol{B} \qquad (2.1)$$

This force is always perpendicular to both the particle velocity and the magnetic field direction. As a result, while the particle's trajectory is deflected, its speed remains unchanged. In this sense, a magnetic field effectively curves the spatial path of a charged particle whenever the field is not aligned with the direction of motion.

Beyond their dynamical influence on charged particles, magnetic fields play a central role in the generation of electrical currents. Faraday demonstrated that an electric current is induced in a conducting loop when the magnetic environment of the loop changes, for instance through the relative motion of a bar magnet toward or away from the conductor. The magnitude of the induced current increases with the rate of change of the magnetic configuration and reverses direction when the magnetic polarity is inverted. Moreover, the induced current scales with the number of turns in the conducting coil. Despite its conceptual simplicity, Faraday's discovery underpins a vast range of technologies that have profoundly shaped modern life.

This phenomenon is formally described by the Faraday–Lenz law, which states that any temporal variation of the magnetic flux Φ through a closed conducting loop induces an electromotive force (emf) e, proportional to the negative time derivative of the flux:

$$e = -\frac{d\Phi}{dt} \qquad (2.2)$$

The negative sign, known as Lenz's law, reflects the fact that the induced emf drives a current whose associated magnetic field opposes the change in magnetic flux through the loop. For a coil composed of *N* identical turns, the total induced electromotive force is amplified accordingly:

$$e = -N\frac{d\Phi}{dt} \qquad (2.3)$$

The induced electromotive force arises from the relative motion between the conductor and the magnetic flux, whether due to motion of the magnetic source, the conductor itself, or a time-varying magnetic field.

Throughout this work, magnets are treated as point magnetic sources, and sensor coils are approximated as point sensors. These assumptions allow a simplified analytical treatment while capturing the essential physics relevant to the proposed measurement approach.

3. DIPOLE MAGNETS

A magnetic dipole represents the simplest configuration of a magnetic source, consisting of two opposite magnetic poles. The magnetic field generated by a fixed dipole located at the origin can be accurately approximated, at distances large compared to its size, by the point-dipole model. At a position vector $\boldsymbol{r}$, the magnetic field is given by (Mahoney et al., 2012; Mahoney & Abbott, 2014):

$$\mathbf{B}_{\text{dipole}}(\mathbf{r}) = \frac{\mu_0}{4\pi}\frac{3(\hat{\boldsymbol{r}}.\boldsymbol{m})\hat{\boldsymbol{r}}-\boldsymbol{m}}{r^3} \qquad (3.1)$$

where μ_0 is the magnetic permeability of free space, $\boldsymbol{m}$ is the magnetic dipole moment, and $\hat{\boldsymbol{r}}$ is the unit vector in the direction of $\boldsymbol{r}$.

Although a static dipole field does not constitute the full solution for a rotating dipole in vacuum, the present study focuses on electromotive force (emf) generation, for which only the relative motion between the magnetic source and the sensing coil is relevant. Under this assumption, the point-dipole approximation of expression (3.1) is sufficient.

For a uniformly magnetized spherical body of mass M and radius R, the absolute value of the magnetic dipole moment is given by:

$$m = \frac{4}{3}\pi MR^3$$

which is equivalent to that of a point dipole located at the center of the sphere.

3.1. Dipole Magnetic Field in Spherical Coordinates

In a spherical coordinate system whose polar axis is aligned with the dipole moment, the magnetic field components of a dipole with moment m_d are expressed as (Castañer et al., 2006):

$$\begin{cases} \boldsymbol{B} = B_r\hat{\boldsymbol{u}}_r + B_\theta\hat{\boldsymbol{u}}_\theta \\ B_r = \dfrac{\mu_0}{2\pi}\dfrac{m_d cos\theta}{r^3} \\ B_\theta = \dfrac{\mu_0}{4\pi}\dfrac{m_d sin\theta}{r^3} \end{cases} \qquad (3.2)$$

where θ is the angle between the dipole axis and the observation direction, and $\hat{\boldsymbol{u}}_r$ and $\hat{\boldsymbol{u}}_\theta$ are the radial and tangential unit vectors, respectively.

A rotating magnetic dipole acquires an effective electric charge q, that depends on its dipole moment m_d and angular velocity ω (Voytsehovich, 2013):

$$q = \frac{2m_d\omega}{3c^2} \qquad (3.3)$$

3.2. Bipolar Waveforms generated by a Rotating dipole

Electromagnetic induction forms the basis of electric generators and rotating machines. An emf is induced in a conducting loop only when magnetic flux through the loop varies in time. Maximum induction occurs when the conductor cuts magnetic field lines perpendicularly.

3.2.1. Rotation axis perpendicular to the dipole moment

Consider a dipole magnet whose magnetic moment is aligned with the z-axis and rotates at angular speed $\omega = \frac{d\theta(t)}{dt}$ about an axis perpendicular to this moment (Fig.3.1). A fixed conducting loop C_1, with axis the z-axis, experiences a time-varying magnetic flux.

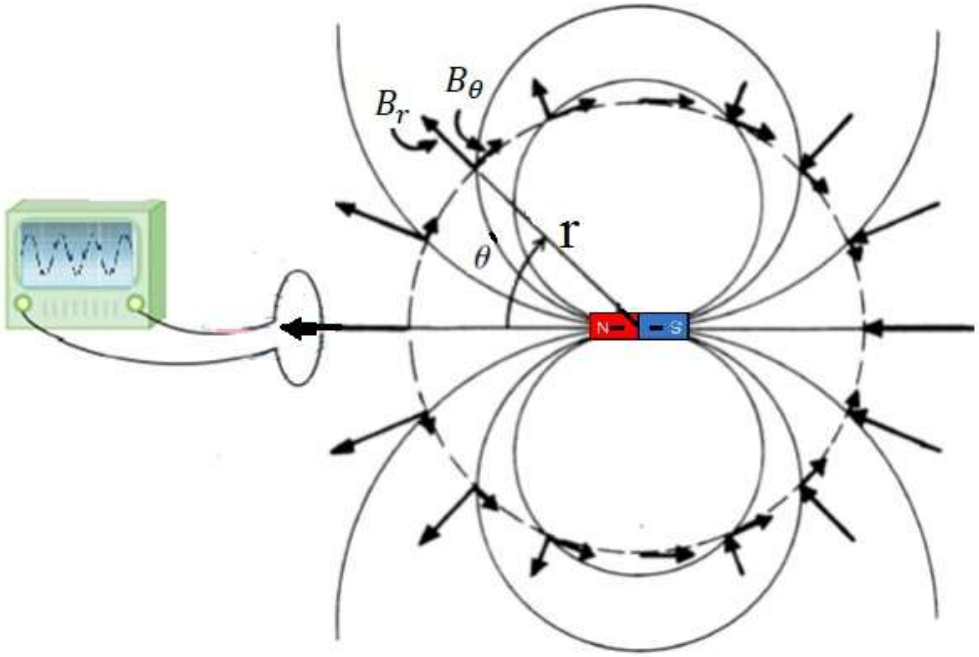

Fig. 3.1. The conversion of relative motion between a circuit and a magnet into emf.

When the magnet rotates, one sinusoidal waveform is produced, with one cycle of the waveform being produced for each complete revolution of the dipole. The output signals from the coil depends on the speed at which the magnet rotates in front of the coil, the strength of the magnetic field at the poles and the characteristics of the coil. The magnetic flux Φ_1 through C_1 is:

$$\Phi_1(t) = AB_r = Ab\cos\theta \qquad (3.4)$$

with,

$$b = \frac{\mu_0}{2\pi}\frac{m}{r^3} \qquad (3.5)$$

where A is the loop area. The induced emf becomes:

$$e_1 = -\frac{d\Phi_1(t)}{dt} = Ab\sin\theta(t)\frac{d\theta(t)}{dt} \qquad (3.6)$$

If a second loop C_2, perpendicular to C_1 and to the plane of the fig.3.1, is introduced, the magnetic flux through it is:

$$\Phi_2(t) = AB_\theta = \frac{1}{2}Ab\sin\theta, \qquad (3.7)$$

leading to an induced emf:

$$e_2 = -\frac{d\Phi_2(t)}{dt} = -\frac{1}{2}Ab\cos\theta(t)\frac{d\theta(t)}{dt} \qquad (3.8)$$

For constant angular velocity, the induced emfs reduce to:

$$e_1 = Ab\omega \sin(\omega t) \qquad (3.9)$$

$$e_2 = -\frac{1}{2}Ab\omega \cos(\omega t) = \frac{1}{2}Ab\omega \sin\left(\omega t - \frac{\pi}{2}\right) \qquad (3.10)$$

The resulting signals are pure sinusoidal waveforms with frequency $f_b = \omega/2\pi$. Increasing or decreasing ω leads to corresponding changes in frequency and amplitude, producing undamped or damped sinusoidal signals (Figs. 3.2–3.4).

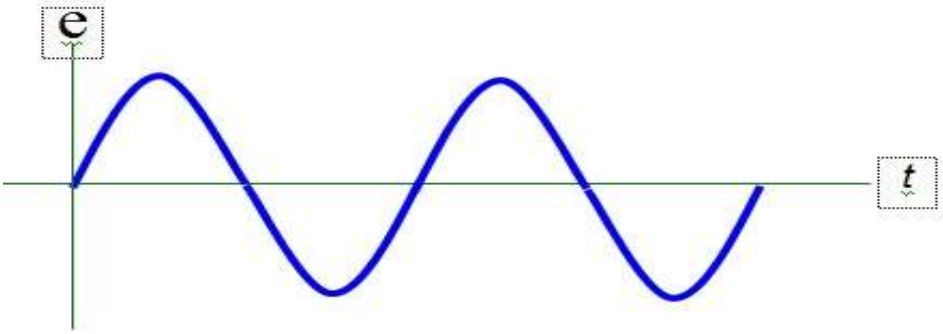

Fig.3.2. Undamped pure sinusoid waveform

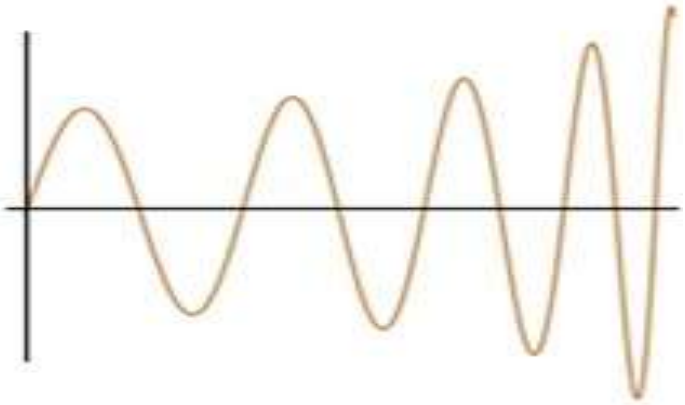

Fig. 3.3. A sinusoidal waveform with increasing frequency and increasing phase

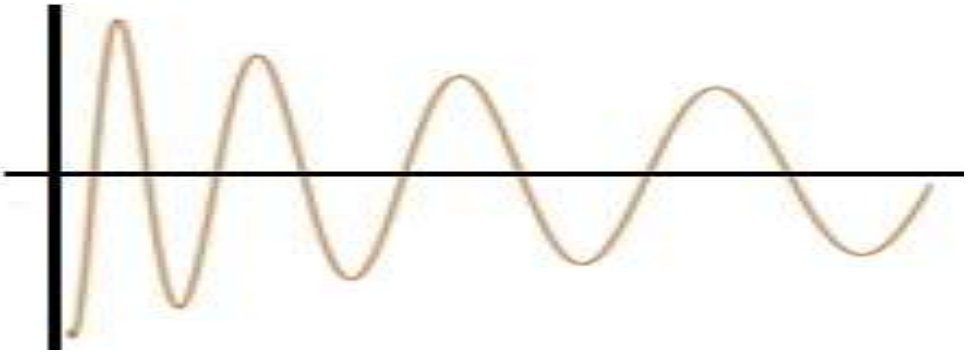

Fig. 3.4. A dumped sinusoidal waveform with decreasing frequency

If the sensing coil is displaced by an angle i relative to the dipole axis (Fig.3. 5), the induced emfs can be expressed as linear combinations of e_1 and e_2. It follows that the general response can always be reconstructed from the previous case $i = \frac{\pi}{2}$, which is therefore sufficient for analysis.

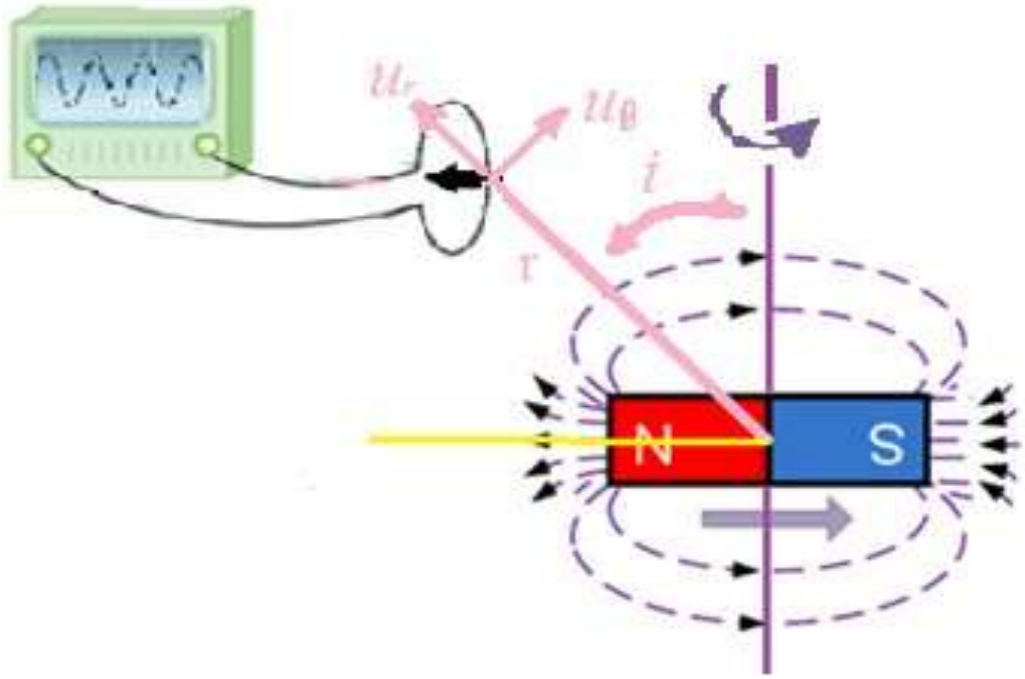

Fig.3.5. The coil placed at a position $\boldsymbol{r}$ *deviated from the z-axis*

3.2.2. Rotation axis aligned with the dipole moment

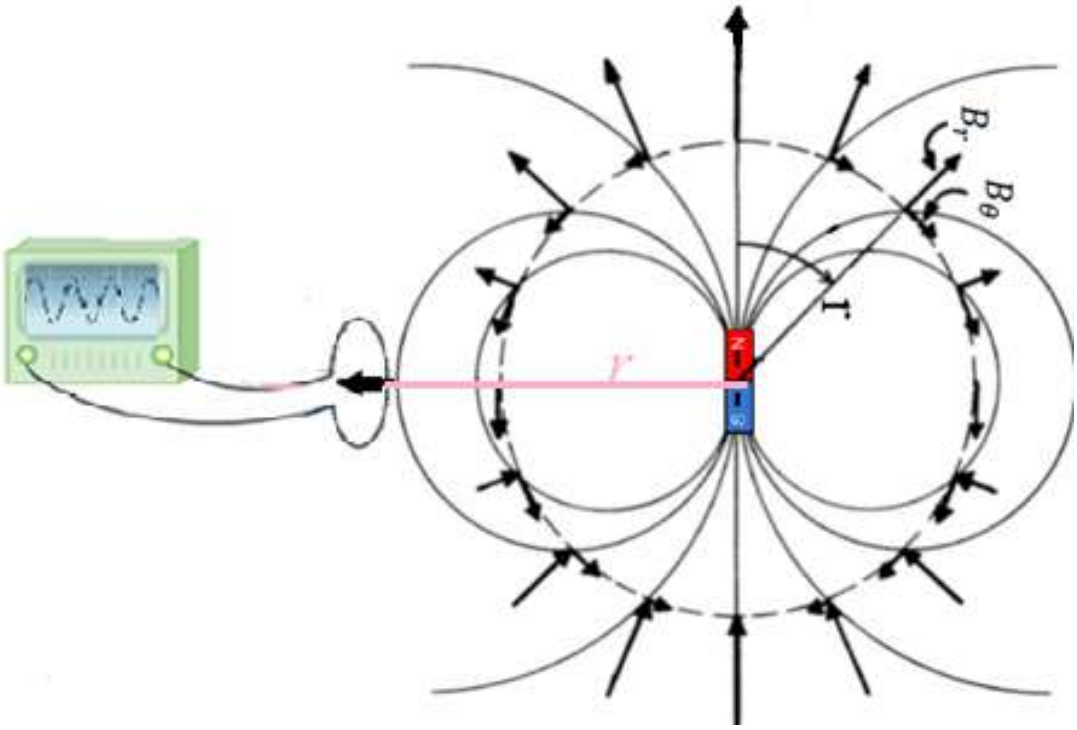

Fig.3.6. The magnet rotates around its magnetic dipole moment, perpendicular to C_1 *-axis*

If the magnet rotates about its own magnetic dipole axis (Fig.3.6), the magnetic flux through both sensing coils remains constant:

$$\Phi^{\parallel}{}_1(t) = 0,\ \Phi^{\parallel}{}_2(t) = AB_{\theta=\frac{\pi}{2}} = \frac{1}{2}Ab \qquad (3.11)$$

In this configuration, no time-varying flux is produced and no emf can be detected, regardless of the observer's position. A dipole rotating about its own axis is therefore electromagnetically silent to stationary coils.

3.2.3. Oblique Rotation Axis

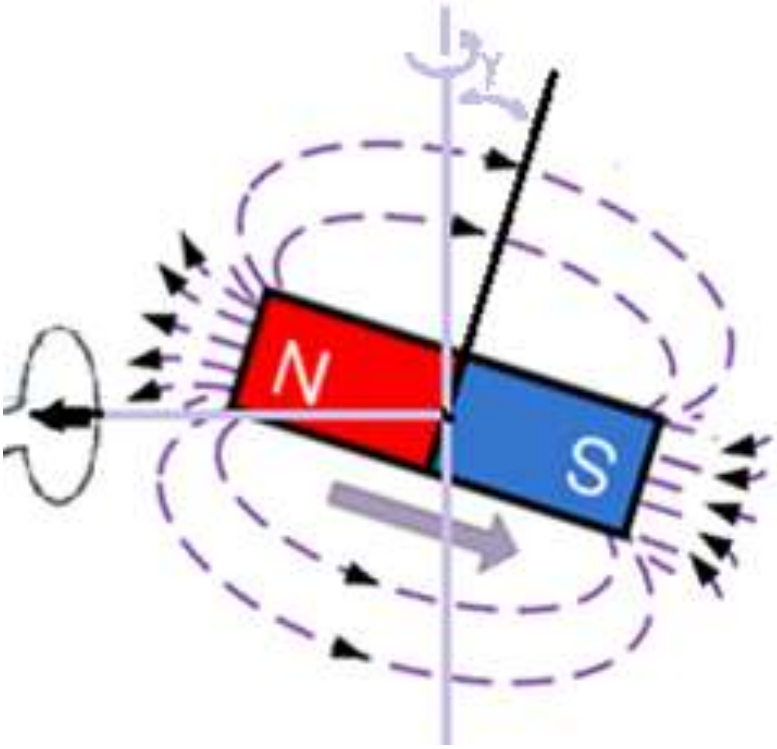

Fig.3.7. A tilt axis of rotation

For a rotation axis inclined by an angle $\gamma \in \left]0, \frac{\pi}{2}\right[$ relative to the dipole moment (Fig.3.7), the induced emf remains sinusoidal but with reduced amplitude:

$$e_{max}(\gamma) = e_{max}(0)cos(\gamma) \qquad (3.12)$$

If γ varies with time while ω remains constant, the waveform exhibits amplitude modulation without frequency change (Figs. 3.8 & 3.9). Thus, changes in the orientation of the dipole affect signal amplitude but not frequency.

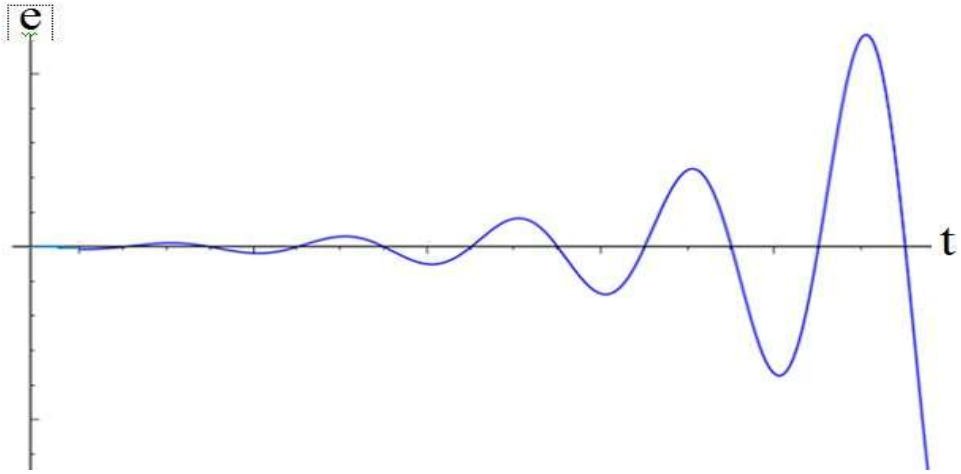

Fig.3.8. Sinusoidal waveform with the same frequency, but with an increasing amplitude

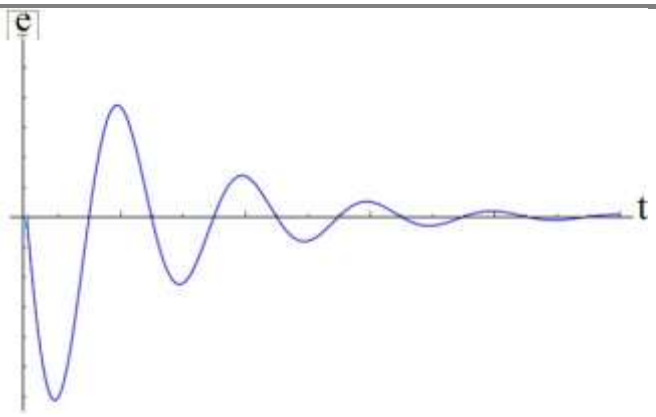

Fig.3.9. A damped sinusoid waveform, with the same frequency

3.3. Elliptically polarized magnetic field generated by a rotating source

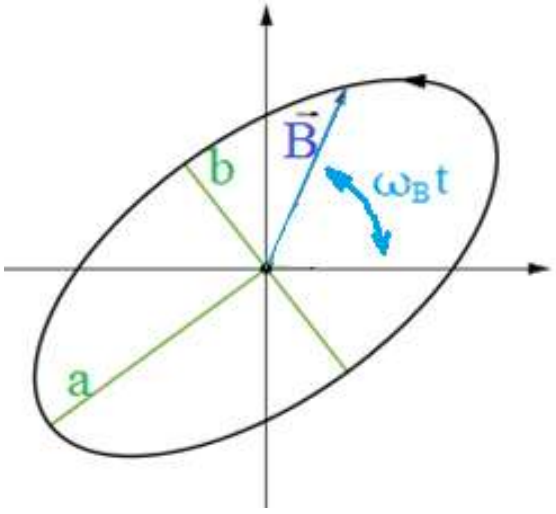

*Fig.3.10. The magnetic field generated by a rotating magnetic dipole***.**

When a magnetic dipole rotates with angular velocity **Ω** such that its dipole moment **m** remains perpendicular to the rotation axis, the magnetic field $\boldsymbol{B}$ at a fixed position traces an ellipse (Fig.3.10). The field extrema are given by (Mahoney et al. 2012):

$$b = B_{min} = \frac{\mu_0|\vec{\mathrm{m}}|}{4\pi r^3} \qquad (3.13.a)$$

$$a = B_{max} = \frac{\mu_0|\vec{\mathrm{m}}|}{4\pi r^3}\sqrt{1+3|r_{\Omega^\perp}|^2} \qquad (3.13.b)$$

The vector $\boldsymbol{r}_{\Omega^\perp} = (Id - \hat{\boldsymbol{\Omega}}\hat{\boldsymbol{\Omega}}^T)\hat{\boldsymbol{r}}$ is the projection of $\hat{\boldsymbol{r}}$ onto the plane perpendicular to **Ω** (the plane in which **m** resides).

The angular velocity vector of the generated magnetic field ($\boldsymbol{\omega}_B$), the actuator's rotation axis (**Ω**), and the position vector ($\boldsymbol{r}$) are all coplanar (Mahoney *et al.* 2012; Mahoney *&* Abbott 2014). Consequently, the generated magnetic field traces an ellipse within a plane perpendicular to the ($\boldsymbol{\Omega}, \boldsymbol{r}$) plane. This rotating magnetic dipole thus produces an elliptically polarized magnetic field. Special cases include circular polarization when $\boldsymbol{\Omega} \parallel \boldsymbol{r}$. In this state, the magnetic vector traces a perfect circle. Moving off-axis **Ω** introduces greater eccentricity as the relative magnitudes of the field components shift. At a fixed distance r, the field's polarization oscillates: starting as a circle, stretching into an ellipse of increasing eccentricity, and then returning to a circular profile.

The generated field magnitude at any position satisfy (Mahoney *et al.* 2012):

$$|\vec{B}| = \frac{\mu_0 |\vec{\mathrm{m}}|}{4\pi r^3}\sqrt{1+3(\hat{m}^T\hat{r})^2} \qquad (3.14)$$

It rotates with angular velocity $\boldsymbol{\omega}_B$ satisfying (Mahoney & Abbott 2014):

$$\|\vec{\omega}_B\| = \frac{B_{min}B_{max}}{\|\vec{B}\|^2}\|\vec{\Omega}\| \qquad (3.15)$$

The distance to the source follows from (*3.13. a*):

$$|\vec{r}| = \left(\frac{\mu_0 |\vec{\mathrm{m}}|}{4\pi B_{min}}\right)^{\frac{1}{3}} \qquad (3.16)$$

This gives a spherical surface of possible locations. To find the direction $\hat{r}$, the angle θ between $\hat{\boldsymbol{m}}$ and $\hat{\boldsymbol{r}}$ is calculated from (3.14):

$$cos^2\theta = (\hat{\boldsymbol{m}}^T\hat{\boldsymbol{r}})^2 = \frac{1}{3}\left(\left(\frac{4\pi B r^3}{\mu_0 m}\right)^2 - 1\right) \qquad (3.17)$$

This gives four possible solutions for θ: $\theta_1, -\theta_1, \theta_1 - \pi, \pi - \theta_1$

3.4. Dipole–Dipole Interaction

Magnetic dipoles interact through the magnetic fields they generate. A dipole $\boldsymbol{m}_d$ placed in an external field $\boldsymbol{B}$ experiences a torque (Mahoney & Abbott 2014):

$$\boldsymbol{\tau} = \mu_0 \boldsymbol{m}_d \times \boldsymbol{B} \qquad (3.18)$$

which tends to align the dipole with the field direction (fig.3.11.b). Prior to alignment, the dipole precesses (fig.3.11.a) around $\boldsymbol{B}$ at the Larmor frequency:

$$f = \gamma\|\vec{B}\| \qquad (3.19)$$

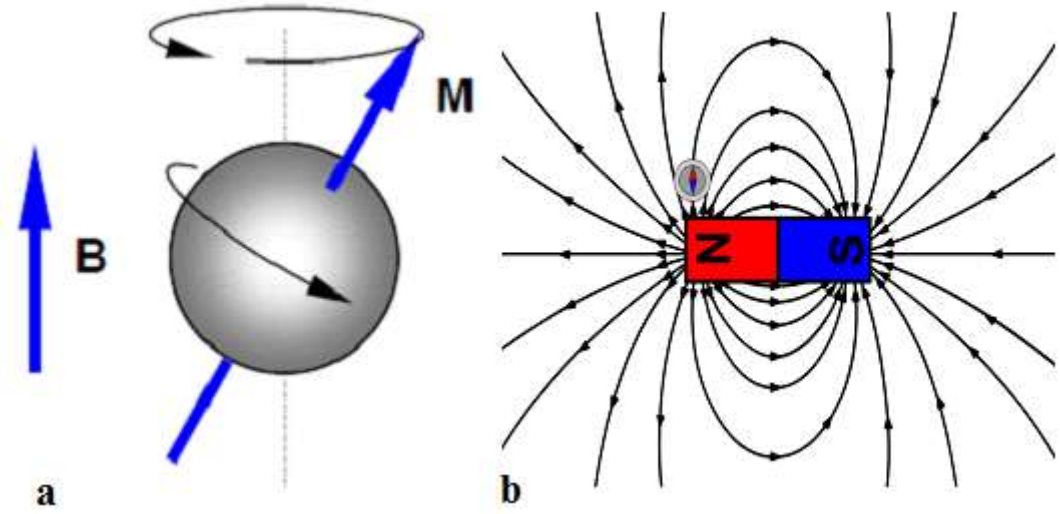

Fig.3.11. (a) The particle precession. (b) The deflection of a compass needle to align with the magnetic field.

When the magnetic field $\boldsymbol{B}$ varies spatially, a magnetic dipole experiences an induced force $\vec{F}$ proportional to the field gradient, which tends to translate the dipole toward regions of stronger magnetic field (Mahoney & Abbott 2014):

$$\boldsymbol{F} = \mu_0(\boldsymbol{m}_d.\boldsymbol{\nabla})\boldsymbol{B} \qquad (3.20)$$

This force drives the translational motion of the dipole, with both its magnitude and direction determined by the dipole moment $\boldsymbol{m}_d$ and the local spatial derivatives of the magnetic field $\boldsymbol{B}$.

The force between two dipoles a and b separated by distance r is given by (Yung et al. 1998):

$$\boldsymbol{F}_{ab} = -\nabla(-\boldsymbol{B}_{ab}.\boldsymbol{m}_b) = \frac{\mu_0}{4\pi}\nabla\left[\frac{3(\hat{\boldsymbol{r}}.\boldsymbol{m}_a)\hat{r} - \boldsymbol{m}_a}{r^3}.\boldsymbol{m}_b\right]$$

$$= \frac{3\mu_0}{4\pi r^4}\{(\hat{\boldsymbol{r}} \times \boldsymbol{m}_a) \times \boldsymbol{m}_b + (\hat{\boldsymbol{r}} \times \boldsymbol{m}_b) \times \boldsymbol{m}_a - 2\hat{\boldsymbol{r}}(\boldsymbol{m}_a.\boldsymbol{m}_b)$$

$$+ 5\hat{\boldsymbol{r}}[(\hat{\boldsymbol{r}} \times \boldsymbol{m}_a).(\hat{\boldsymbol{r}} \times \boldsymbol{m}_b)]\} \qquad (3.21)$$

Leading to attraction or repulsion depending on their relative orientation. At the "magic angle" $\theta = 54.73°$ ($3\cos^2\theta - 1) = 0$ *(fig.3.12)*, the force vanishes (Castañer et al., 2006).

For two aligned dipoles of equal moment m, Eq. (3.21) reduces to (Castañer et al., 2006):

$$B = \frac{\mu_0}{2\pi}\frac{m}{r^3}u_z \qquad (3.22)$$

The force between the two dipoles reduces to (Castañer et al., 2006):

$$F = \pm\frac{\mu_0}{2\pi}\frac{3m^2}{r^4}u_z \qquad (3.23)$$

where the sign depends on whether the dipoles are parallel or antiparallel. A detailed physical interpretation of the resulting motion is given by Solomon (1955).

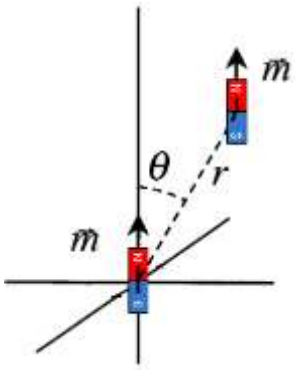

Fig.3.12. Two equal magnetic dipoles with parallel moments

While dipole magnetic fields provide the simplest framework for understanding field topology, polarization, and temporal modulation, they represent only the lowest-order term in the multipolar expansion of realistic magnetic sources. Many physical systems—both in laboratory devices and astrophysical environments— exhibit magnetic configurations that deviate significantly from pure dipolar symmetry. In particular, quadrupolar fields introduce spatial gradients and field reversals that fundamentally modify the induced signals and their detectability. Building on the dipole analysis presented above, we now extend the formalism to quadrupole magnetic fields, examining their structure, polarization properties, and implications for direct magnetic field sensing.

4. QUADRUPOLES

Quadrupole magnets constitute the second most important class of magnetic elements after dipoles and are widely used in particle accelerators, focusing systems, and beam optics. For example, more than 1100 quadrupole magnets of various designs are employed in the Large Hadron Collider (LHC) at CERN.

Conceptually, a magnetic quadrupole may be regarded as a superposition of two magnetic dipoles arranged with opposite polarity.

The magnetic field generated by a quadrupole of strength Q can be expressed in spherical coordinates as (Cunha 2006):

$$\begin{cases} \boldsymbol{B} = B_r \hat{\boldsymbol{u}}_r + B_\theta \hat{\boldsymbol{u}}_\theta \\ B_r = \dfrac{9Q}{8r^4}\left(cos2\theta + \dfrac{1}{3}\right) \\ B_\theta = \dfrac{3Q}{4r^4} sin2\theta \end{cases} \qquad (4.1)$$

Where r and θ are the usual spherical coordinates and $\hat{\boldsymbol{u}}_r$ and $\hat{\boldsymbol{u}}_\theta$ are the corresponding unit vectors.

4.1. Quadripole-induced Waveforms

Unlike dipoles, which possess two magnetic poles, a quadrupole has four poles—two north and two south. As a result, each full rotation of a quadrupole produces two complete cycles of magnetic field variation. Consequently, the characteristic frequency of the induced emf is:

$$f_q = 2\, f_b = \frac{\omega}{\pi}, \qquad (4.2)$$

where ω is the angular velocity of rotation. The induced waveforms are therefore similar in form to those generated by dipoles, but with twice the number of cycles per revolution.

4.1.1. Rotation Axis Perpendicular to the Quadrupole Moment

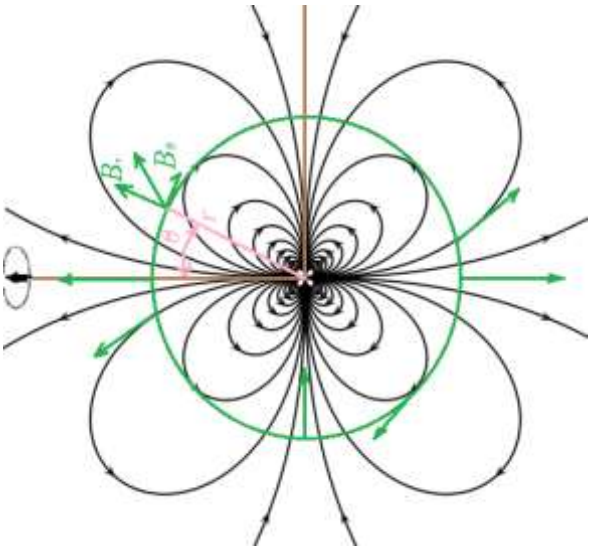

Fig. 4.1. A coil C_1 of horizontal axis placed in front of a rotating quadrupole

Consider a quadrupole magnet rotating at angular speed ω about an axis perpendicular to its magnetic moment and passing through its center (Fig.4.1). A fixed single-loop conductor C_1 is placed in front of the rotating magnet.

After a rotation by an angle θ, the magnetic flux Φ_{1q} linked with C_1 is

$$\Phi_{1q}(t) = AB_r = 3Ab\left(cos2\theta + \frac{1}{3}\right) \qquad (4.3)$$

where,

$$b = \frac{3Q}{8r^4} \qquad (4.4)$$

and A is the loop area. The induced emf is then

$$e_{1q} = -\frac{d\Phi_{1q}(t)}{dt} = 6Absin2\theta(t)\frac{d\theta(t)}{dt} \qquad (4.5)$$

If a second coil C_2, perpendicular to C_1 and the plane of the figure, is introduced, the magnetic flux Φ_{2q} becomes

$$\Phi_{2q}(t) = -AB_\theta = -2Absin2\theta \qquad (4.6)$$

leading to an induced emf

$$e_{2q} = -\frac{d\Phi_{2q}(t)}{dt} = -4Abcos2\theta(t)\frac{d\theta(t)}{dt} \qquad (4.7)$$

For constant angular velocity $\omega = \frac{d\theta(t)}{dt}$, the induced emfs reduce to

$$e_{1q} = 6Ab\omega sin2(\omega t) \qquad (4.8)$$

$$e_{2q} = -4Ab\omega cos2(\omega t) = 4Ab\omega \sin\left(2\omega t - \frac{\pi}{2}\right) \qquad (4.9)$$

These signals are pure sinusoidal waveforms with constant phase and frequency $f_q = \omega/\pi$ (fig.3.2), and a phase shift of $\frac{\pi}{2}$ between the two coils. As in the dipole case, increasing (or decreasing) ω results in higher (or

lower) frequency and amplitude (fig.3.3 & 3.4).

If the sensing coils are displaced by an angle $i \in \left]0, \frac{\pi}{2}\right[$ relative to the quadrupole axis, the induced emfs become linear combinations of e_{1q} and e_{2q}. Consequently, the general response can always be reconstructed from the case $i = \frac{\pi}{2}$ (the previous situation), which is sufficient for analysis.

4.1.2. Rotation axis aligned with the Quadrupole moment

If the quadrupole rotates about its own magnetic moment, the magnetic flux through both coils remains constant and no time-varying component is produced. As a result, no emf is detected, regardless of the detector position. A quadrupole rotating about its symmetry axis is therefore electromagnetically silent to fixed antennas.

4.1.3. Oblique Rotation Axis

When the rotation axis forms a fixed angle $\gamma \in \left]0, \frac{\pi}{2}\right[$ with the quadrupole moment, the induced waveform remains sinusoidal, but its amplitude is reduced by a factor $\cos(\gamma)$. Variations of γ with time lead to amplitude modulation while preserving the signal frequency, producing either growing or damped sinusoidal waveforms (Figs. 3.8 & 3.9).

4.1.4. Off-Center Rotation

If the quadrupole rotates about an axis that does not pass through its center, additional asymmetries arise in the magnetic flux variation, leading to more complex induced waveforms (Fig.4.2). Such signatures may provide diagnostic information on the geometry and stability of the rotating system.

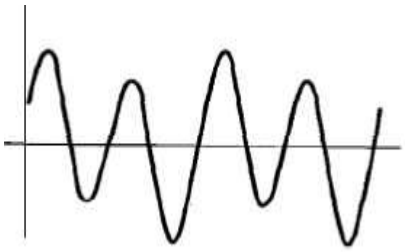

Fig.4.2. Waveform from coil censing an off-center rotating quadrupole

4.1.5. Example: Waveforms from Merging Dipoles

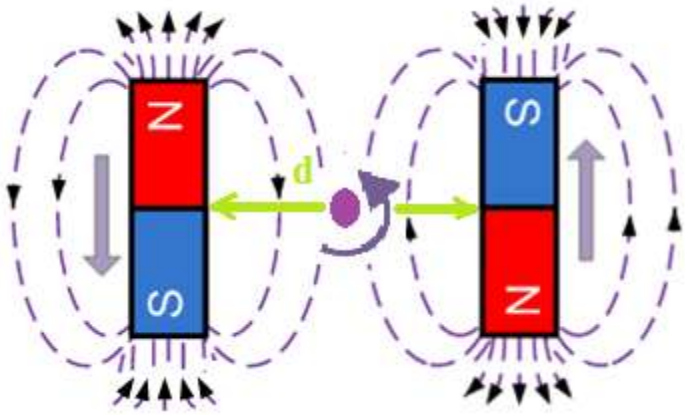

Fig.4.3. Two antiparallel identical dipoles, orbiting each other.

As an illustrative example, consider two identical antiparallel dipoles, separated by a distance d, orbiting each other in a plane containing their magnetic moments (Fig.4.3). Mutual magnetic attraction and torque cause the system to spiral inward, increasing the rotation rate until the dipoles merge into a single effective dipole. During this inspiral phase, the detected waveform exhibits a continuously increasing frequency.

Following merger, the resulting dipole may precess and reorient until its magnetic moment becomes perpendicular to the orbital plane, at which point the magnetic field becomes stationary with respect to the detector and no further signal is observed. A representative waveform for such an event is shown in Fig.4.4.

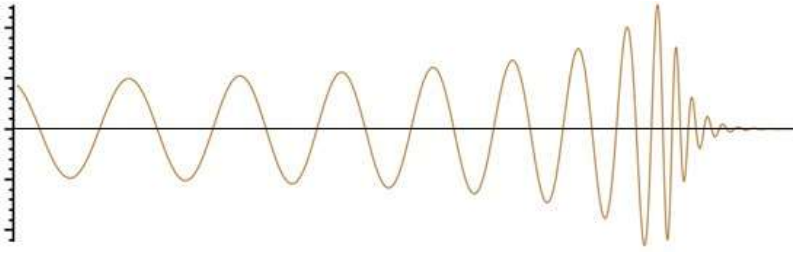

Fig.4.4. A waveform of two dipoles merging in one dipole after a spiraling phase.

4.2. Polarization of Quadrupole Magnetic Fields

A quadrupole rotating about an axis perpendicular to its plane generates a magnetic field that is elliptically polarized at every point in space. Using relations (*4.1*), it follows that

ISSN No. 2454-6194 | DOI: 10.51584/IJRIAS |Volume XI Issue February 2026
Special Issue on Innovations in Environmental Science and Sustainable Engineering

$$\left(\frac{8r^4}{9Q}\right)^2\left(B_r-\frac{1}{3}\right)^2+\left(\frac{4r^4}{3Q}\right)^2(B_\theta)^2=cos^2 2\theta+sin^2 2\theta=1 \qquad (4.10)$$

Thus, the magnetic field traces an ellipse, with one complete ellipse generated every half rotation of the quadrupole.

5. MAGNETIC FIELD SENSORS

5.1. The harmonic coil method

One of the most accurate and widely adopted techniques for characterizing the magnetic field of fixed accelerator magnets is the rotating (harmonic) coil method, in which the sensing coils typically rotate at speeds up to about 10 revolutions per second.

The use of orthogonal coils for magnetic field sensing is well established. In the harmonic coil technique, two coils—capable of oscillatory motion—are mounted perpendicular to each other and rotated within the static magnetic field of the magnet under investigation. This configuration provides a convenient and precise means of determining the coefficients of a static quadrupole field. A commonly employed geometry consists of one coil oriented in the radial direction (C_r) and the other in the tangential direction (C_θ), as illustrated in Fig.5.1.

As the coils rotate through the magnetic field, an alternating current is induced in the conductors. This current generates a magnetic field that opposes the external static field, producing a Lorentz force that causes a mechanical displacement of the coils from their equilibrium positions. The resulting displacement is directly proportional to the Lorentz force and therefore to the local components of the magnetic field. By analyzing these oscillations, the spatial structure and strength of the quadrupole field can be accurately reconstructed (Walckiers, 2011).

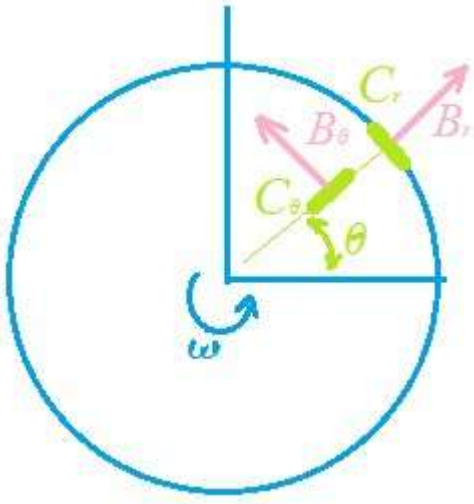

Fig.5.1. Two coils are perpendicular to each other. (C_θ) in the tangential direction and (C_r) in the radial direction

5.2. The fixed orthogonal coil method

For measurements of a generating magnetic quadrupole field, the same physical principles apply whether the magnet is rotated relative to fixed sensing coils or, equivalently, whether the coils are rotated within a fixed magnetic field. In both cases, the measurable signal arises from the relative motion between the magnetic field source and the detectors.

An alternative approach, which has also been experimentally explored, consists in inducing rotation of the magnetic field itself while keeping the sensing coils fixed. The resulting time-varying magnetic flux through the coils generates output signals that can be used to infer the position and orientation of the quadrupole field relative to the detectors. In the absence of such relative motion, the method becomes ineffective, as no flux variation is produced.

The amplitude of the detected signal modulation depends sensitively on the orientation of the sensing coils with respect to the quadrupole's rotation axis, providing additional information on the geometry and alignment of the magnetic source.

6. APPLICATION TO ASTRONOMY

Magnetic fields are fundamental actors throughout stellar formation, evolution, and death, yet their direct detection remains extremely challenging.

Stellar surface magnetic fields are most commonly inferred indirectly through spectropolarimetric diagnostics, notably via the Zeeman effect and polarization signatures in spectral lines (Kochukhov 2015). These techniques reconstruct magnetic maps through inversion methods rather than through direct field measurements. In this section, we examine how the first direct detection of magnetic field gradients associated with compact-object mergers, achieved in September 2015, can be interpreted within the framework developed in this work.

6.1. Dead stars and magnetic fields

Compact stellar remnants—white dwarfs, neutron stars, and black holes—are frequently associated with intense magnetic fields, often sustained or amplified by rapid rotation. Magnetars, a subclass of neutron stars, are believed to host the strongest magnetic fields known in nature, with surface field strengths typically ranging from 10^8 to 10^{11} T, and potentially reaching values as high as 10^{14} T (Sinha & Mukhopadhyay, 2013).

At distances much larger than the stellar radius, the magnetic field generated by such objects is well approximated by a dipolar configuration (Marklund et al. 2000), given by

$$\mathrm{B}(r) = \frac{B_s r_p^3}{\mathrm{r}^3}, \qquad (6.1)$$

where B_s is the surface magnetic field and r_p the stellar radius.

The nearest star to the Solar System, Proxima Centauri, lies at a distance of approximately 4.24 light-years

(≈270 000 UA). Even assuming the most extreme magnetic fields known for magnetars, the dipolar field strength reaching Earth from any compact star is vanishingly small. A straightforward estimate shows that the resulting field amplitude at Earth would be far below

$$\frac{B_s}{10\mathrm{r}^2} << \frac{10^{13}}{27^2 10^8 149^2 10^{18}} = \frac{1}{27^2 149^2} 10^{-13} < 10^{-18} T, \qquad (6.2)$$

well beneath the sensitivity of even the most advanced classical magnetometers.

Superconducting Quantum Interference Devices (SQUIDs) are the most sensitive conventional instruments available for magnetic field measurements, capable of detecting fields down to 10^{-14} T. When measurements are averaged over long integration times, sensitivities can approach the 5.10^{-18} T level. In practice, commercial SQUID magnetometers operate by measuring variations in magnetic flux rather than absolute magnetic field amplitudes (Buchner et al., 2018). Nevertheless, these limits imply that direct detection of static or slowly varying stellar magnetic fields at Earth is fundamentally impossible using classical magnetometry.

6.2. Binary mergers as time-varying magnetic sources

The situation changes dramatically in the case of compact binary systems. When a massive star undergoes core collapse in a supernova, the remnant may form either a neutron star (NS) or a black hole (BH). Modeling each compact object as an effective magnetic dipole, dipole–dipole interactions (paragraph 3.4.) can give rise to a rotating binary configuration, potentially culminating in a merger.

The evolution of such binaries proceeds through three well-defined stages: inspiral, merger (or plunge), and ringdown (Kun et al., 2014). During the inspiral phase, the orbital separation steadily decreases while the orbital frequency increases, leading to rapidly time-varying magnetic configurations and strong magnetic field gradients.

6.3. Observational breakthrough: September 2015

On 14 September 2015, the Advanced LIGO detectors made the first direct observation of transient signals associated with a compact binary merger. The signal, later designated GW150914, originated from the coalescence of two black holes BHs and spanned frequencies from approximately 20 Hz to 450 Hz.

Such signals are far too weak and too rapid to be detected by classical magnetometers. However, their rapidly varying nature enables detection through instruments capable of responding to magnetic field gradients rather than absolute field amplitudes.

6.4. The Laser Interferometer Gradient Magnetic Field Observatory

Modern laser interferometers, derived from the Michelson–Morley concept, were initially designed to detect minute differential displacements between orthogonal arms. Large-scale installations such as GEO600 in Germany, LIGO in the USA, Virgo in Italy, KAGRA, and TAMA300 in Japan are rigidly anchored to Earth's crust and employ freely suspended mirrors as test masses.

Some of these detectors made observations between 2002 and 2011, but no fringe shifts were observed (LSC and VIRGO, http://www.ligo.org).

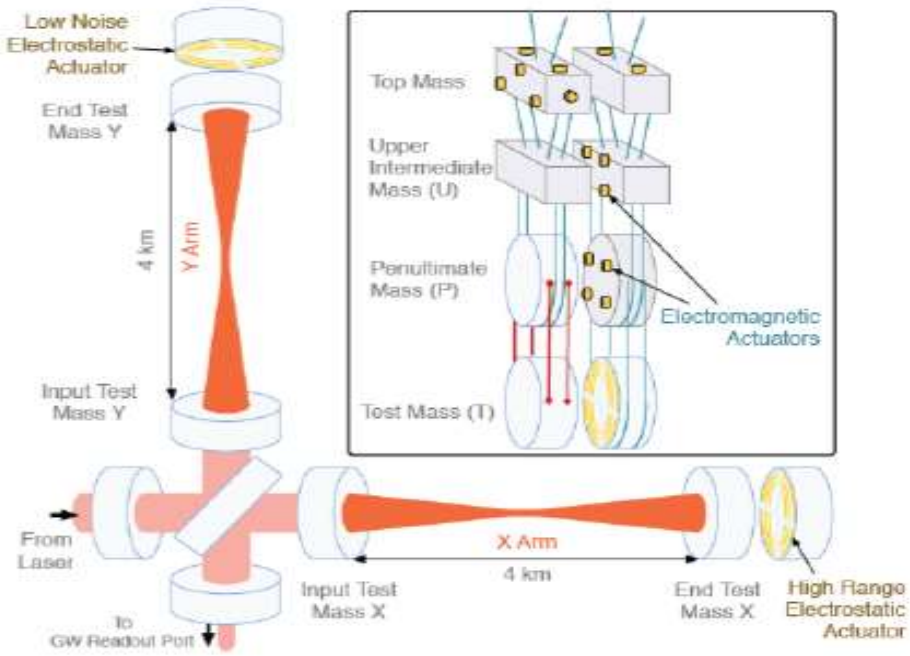

Fig.6.1. Simplified diagram of an Advanced LIGO interferometer (https://dcc.ligo.org/LIGO)

The Advanced LIGO upgrade, initiated in 2010, significantly enhanced the interferometer's sensitivity by incorporating two highly reflective, free-falling test mass mirrors positioned perpendicularly along 4-km arms—

a scale over 300 times longer than the original Michelson design. To achieve the extreme precision required for gravitational wave detection, these mirrors are integrated with sophisticated electromagnetic circuits, specifically magnet-coil actuators or electrostatic drives (ESDs). As illustrated in Figure 6.1., these components provide nanometric control over the mirrors' position and orientation, allowing for the sub-atomic stability necessary to observe the faintest ripples in spacetime (Effler et al., 2015; Abbott et al. 2019).

Any time-varying magnetic flux through these coils induces eddy currents via Faraday's law, generating local magnetic field gradients that exert forces on the mirrors (Cirone et al. 2018; Effler et al., 2015; Abbott et al., 2016b). These forces produce mirror displacements (ΔL) that are linearly proportional to the applied force and are directly measurable via laser interferometry (Biwer et al*.,* 2017).

This laser interferometric sensor has been rigorously validated for its ability to accurately measure mirror displacement induced by magnetic field gradients (Michimura et al. 2017; Thrane et al. 2013).

Remarkably, magnetic field gradients as small as a few tens of picotesla can induce mirror displacements of order 2×10^{-18} m, comparable to those produced by astrophysical merger events such as GW150914 (Michimura et al., 2017; Abbott et al., 2016a). A magnetic pulse of 10 pT combined with a coupling factor of 1×10^{-7} m/T produces a strain of approximately $h \approx 2.5 \times 10^{-22}$ (Thrane et al., 2013). The specific relationship between the external magnetic field and this induced strain is frequency-dependent and can be modeled through precise coupling calculations (Abbott et al., 2016b).

These gradients can induce physical displacement within the detector, and under conditions of high magnetic intensity, they may generate "glitches"—transient noise artifacts that risk being identified as authentic signals from astronomical bodies (Cirone et al., 2018). To distinguish between environmental noise and genuine cosmic events, researchers employ a multi-layered verification process. Since high magnetic gradients can physically nudge the test masses—creating "glitches" that mimic the strain of a gravitational wave—scientists utilize an array of sensitive magnetometers located around the vacuum chambers. By cross-referencing the interferometer's data with these environmental sensors, they can "vet" the signal; if a spike in the magnetic field coincides exactly with a detected displacement, the event is flagged as terrestrial noise and discarded. Furthermore, because a true astronomical wave should appear in multiple detectors (like both LIGO Hanford and Livingston) with a specific time delay and matching waveform, local magnetic glitches can be isolated and filtered out.

6.5. Magnetic noise and gradient sensitivity

Environmental magnetic fluctuations represent a significant noise source for interferometers (Effler *et al.* 2015; Cirone et al. 2018). Two dominant coupling mechanisms are described by

$$F_1 = 2\delta\mu_{mag}\partial_l B, \qquad (6.3)$$

$$F_2 = 2\mu_{mag}\delta(\partial_l B) \qquad (6.4)$$

where μ_{mag} is the magnetic moment of the actuator magnets and $\partial_l B$ the longitudinal magnetic field gradient (Michimura et al., 2017).

The total displacement ΔL observed by the interferometer is a composite of astrophysical signals and background noise; consequently, magnetometers are used to monitor environmental fluctuations, enabling researchers to identify and subtract detectable correlated noise to isolate the genuine signal (Abbott et al., 2016b).

While LIGO was rigorously designed to detect fluctuations in magnetic flux, some critics argue that sensitivity to one phenomenon does not inherently guarantee the accurate capture of another; as the analogy suggests, an apparatus perfected for catching birds is not necessarily equipped to catch ghosts. This distinction has led some researchers to express skepticism regarding the definitive detection of gravitational waves, citing concerns over potential environmental correlations (Szostek et al. 2019). Indeed, such skepticism has historical roots, as even Einstein once doubted whether gravitational radiation would ever be directly detectable.

6.6. Direct detection of waves from astronomical mergers

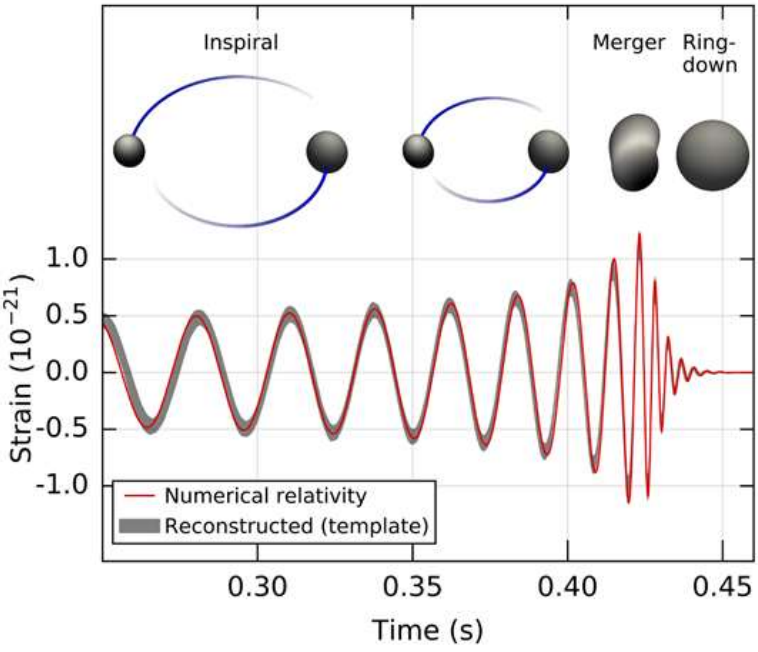

Fig.6.2. GW150914 (LIGO) The instrumental strain data in the Livingston detector

The detection of GW150914 demonstrated that LIGO is capable of sensing extremely weak, rapidly varying signals corresponding to compact binary mergers occurring over cosmological distances (fig.6.2). The final fraction of a second of the merger involves relativistic orbital velocities approaching half the speed of light.

The observed waveform (Fig.6.2) comprises approximately 10 cycles during the inspiral phase, characterized by a frequency sweep from 35 Hz to 150 Hz, followed by the merger and subsequent ringdown. Data surrounding the event were identified as clean and stationary (Abbott et al. 2016b). Furthermore, a comprehensive analysis of environmental variables ruled out all terrestrial or instrumental noise sources capable of mimicking the detector output, confirming that the episode was uniquely consistent with a binary black hole merger (Abbott et al. 2016b). Consequently, GW150914 is verified as a legitimate astrophysical event.

While the absolute amplitude of the magnetic field reaching Earth is negligible, the extreme fluctuations generated by rapid stellar rotation—speeds unattainable in terrestrial laboratories—create significant magnetic field gradients. These rapid variations are the catalyst for detection, providing the signal contrast necessary to overcome the field's inherent faintness. This mechanism induces minute mirror displacements.

GW150914 can be generated by mirror displacements due to experimented rapid change in magnetic fields, or by variation in lengths of the arms generated by theoretical gravitational waves.

6.7. Multimessenger confirmation: GW170817

The detection of GW170817 in August 2017 marked the first observation of a binary neutron star merger. The signals are not obvious in Virgo. Unlike binary black hole events, this signal persisted for approximately 100 seconds and spanned thousands of cycles, beginning at a frequency of 24 hertz. Crucially, it was followed by electromagnetic counterparts across the gamma-ray, X-ray, ultraviolet, optical, infrared, and radio bands (Alexander et al. 2017; Coulter et al. 2017; Abbott et al. 2017; Nicholl et al., 2017; Margutti et al. 2017 ; Ziaeepour, 2019).

This multimessenger detection confirmed that compact binary mergers are powerful sources of rapidly evolving electromagnetic and magnetic phenomena. The temporal coincidence of magnetic-gradient-induced, and electromagnetic signals reinforces the interpretation that the interferometric signal reflects a direct response to extreme, rapidly varying physical fields generated at the source.

7. DISCUSSION AND INTERPRETATION OF THE RESULTS

It is well established that the variations in the arm lengths measured by the LIGO interferometers are triggered by astrophysical events. The recorded waveforms therefore reflect a real, external physical phenomenon acting on the detector.

In all the sensors LIGO/VIRGO/KAGRA, we are able to monitor the length changes by changing the positions of the test masses in the balanced state of electromagnetic forces (Mei & Yu, 2016). LIGO is the most sensible sensor to magnetic field, VIRGO is more shielded than LIGO, KAGRA is the most shielded. KAGRA was not able to detect any signal from astronomical bodies. VIRGO was able to detect only signals from the most massive or the closest to our earth. LIGO is the best sensor of the astronomical signals.

There are two possibilities for the changes in the output of the experiments. The first is that the positions of the test masses remain unchanged, but the lengths of the arms are changed under the space-time curvature caused by GW passage, in the standard opinion of general relativity. There is no concept of force. The second is that the lengths of arms remain unchanged, but the positions of the test masses are changed, under the action of force to cause their vibration.

In this work, we argue that a consistent and physically grounded interpretation of the LIGO readout can be formulated in terms of extremely rapid variations of magnetic field gradients generated during compact-object mergers. Notably, LIGO has been extensively calibrated and experimentally validated for its sensitivity to magnetic-field–induced forces acting on its test masses. While this confirms its capability to detect magnetic gradient variations, it does not automatically imply sensitivity to hypothetical or untested field phenomena of a different physical nature.

7.1. Analysis of the GW170817 Event

Compact stellar remnants—white dwarfs, neutron stars, and black holes—are commonly associated with intense magnetic fields, often sustained or amplified by rapid rotation. For simplicity, each object may be modelled as a point magnetic dipole. When two such compact objects, possessing comparable magnetic moments, approach one another closely (e.g. neutron–neutron, black hole–black hole, or mixed binaries), dipole–dipole interactions naturally arise.

Prior to coalescence, the system may be approximated as two antiparallel dipoles forming an effective quadrupolar configuration within a rotating plane that either contains or is perpendicular to their magnetic moments. In the latter case, the system evolves in a manner qualitatively similar to nonspinning bodies, with a nearly fixed orbital plane in space.

Magnetic interaction forces reduce the separation between the two bodies, while conservation of angular momentum leads to an accelerating inspiral. As the orbital frequency increases, the temporal variation of the magnetic field gradients at Earth also increases, resulting in stronger induced currents and larger test-mass displacements within the interferometer. This mechanism naturally explains the observed growth in both amplitude and frequency during the inspiral phase of the signal (Fig.6.2.).

Following the merger (plunge), the system forms a single compact object. Part of the linear momentum is converted into angular momentum, inducing rapid rotation, while another part may generate a recoil (“kick”) velocity. If this velocity has a component directed away from Earth, the magnetic field amplitude at the detector location decreases, leading to the observed post-peak reduction in signal amplitude despite a continued increase in frequency. Subsequently, the newly formed dipole undergoes precession until its magnetic moment aligns perpendicular to the orbital plane, at which point temporal variations in the magnetic field vanish at the detector location. Once the ringdown phase is complete, no further sinusoidal signal is expected.

Events such as GW170817, GW150914, and GW151226 can be interpreted as manifestations of magnetic interactions operating on astrophysical scales. Given the extreme weakness of stellar magnetic fields at Earth, relativistic orbital velocities are required to generate magnetic field variations rapid enough to be detectable.

This explains why signals are observed during inspiral, merger, and ringdown phases, but not during uniform rotation (Abbott et al., 2016a).

7.2. Conclusion: KAGRA as the Definitive Arbiter of Signal Origin

This study suggests that the signals recorded by the global interferometric network may be fundamentally linked to the magnetic dynamics of compact, fast-rotating astrophysical systems rather than spacetime curvature. The extreme rotational velocities and accelerations reached during the coalescence of magnetized neutron stars or black hole environments generate rapid temporal variations in magnetic flux. While the absolute field strengths at Earth are weak, these high-frequency gradients are capable of inducing electrodynamic forces and physical displacements in the suspended test masses of long-baseline interferometers.

The Comparative Shielding Evidence

A systematic trend emerges when examining the global network: signal strength appears inversely proportional to the degree of magnetic shielding.

- **LIGO:** Possesses the weakest magnetic isolation; consistently records the most pronounced signals.
- **Virgo:** Employs intermediate shielding; detects only high-SNR or extremely massive proximal events, often with significantly fainter data (Abbott et al., 2020).
- **KAGRA:** Utilizes the most extensive magnetic shielding and cryogenic isolation (Yamada 2020). Despite its high theoretical sensitivity, KAGRA has reported no confirmed astrophysical detections to date (Akutsu, et al. 2025).

Ultimately, interferometric observatories appear to function as highly sensitive detectors of relativistic magnetic flux variations, capable of producing signals that closely mimic canonical gravitational-wave waveforms (Kowalska-Leszczyńska et al., 2017). The systematic attenuation and eventual disappearance of these signals with increasing magnetic shielding—from LIGO to Virgo and finally to KAGRA—suggests that a significant electrodynamic contribution may be present in current detections. This trend motivates a reassessment of the physical origin of the observed interferometric responses.

Theoretical concerns regarding the feasibility of unambiguous gravitational-wave detection within the LIGO framework have been previously raised by Ulianov et al. (2016) and Mei & Yu (2016), who argued that isolating pure spacetime curvature effects from other physical interactions presents fundamental challenges. While the physical displacement of the mirrors can be accounted for, the theoretical possibility of a change in arm length resulting from the actual stretching or squeezing of the spacetime fabric remains an open question.

Rather than exclusively treating magnetic effects as noise to be mitigated in order to enhance gravitationalwave sensitivity (Aasi et al., 2012), an alternative approach is to explicitly model and suppress test-mass motion driven by magnetic field gradients and related environmental couplings (Akutsu et al. 2025). Such a strategy would allow a more definitive separation between genuine spacetime strain and non-gravitational physical influences, thereby strengthening the physical interpretation of interferometric signals.

Mathematical Modeling and the Role of KAGRA

Let us now focus on the detected signal from LIGO\VIRGO\KAGRA. The measured strain $\hbar_i(t)$ in the i-th detector can be modeled as the sum of instrumental noise $n_i(t)$, a correlated gravitational wave signal $s_i(t)$ caused by stretching of spacetime, and a correlated signal $M_i(t)$ arising from magnetic gradients, related within mirror motion (s_i and M_i are of astrophysical origin):

$$h_i(t) = n_i(t) + M_i(t) + s_i(t) \qquad (7.1)$$

Because KAGRA is effectively shielded against these magnetic gradients ($M_{\mathrm{KAGRA}}(t) \approx 0$), its lack of detection ($s_{\mathrm{KAGRA}}(t) \approx 0$) serves as a critical control. If the signals were purely gravitational, they would persist regardless

of electromagnetic shielding (then $s_{\mathrm{KAGRA}}\ (t) \neq 0$). The fact that detections vanish as shielding improves suggests that the "astronomical signal" (s_i+M_i) is electrodynamic in nature ($s_i \approx 0$). Consequently, KAGRA is the most vital apparatus for deciding on the final conclusion; its silence provides the empirical evidence needed to distinguish between mirror motion caused by (experimented) magnetic flux and the theoretical stretch of spacetime caused by gravitational waves (never experimented before).

Instrumental Ambiguity and Frequency Vetoes

A fundamental ambiguity remains because both gravitational waves and varying magnetic fields can theoretically produce indistinguishable modulations at the photodiode. This is exacerbated by the limited bandwidth and sensitivity of on-site magnetometers in LIGO and Virgo. These systems are optimized to veto low-frequency terrestrial noise; however, they are poorly adapted to handle astronomical signals exceeding 30 Hz—particularly near the 60 Hz power line oscillation frequency in the US. This technical constraint likely restricts the search frequency range (Abbott et al. 2016b), masking the fact that the "vetoed" terrestrial noise and the "detected" astronomical signals may share a common magnetic origin.

Final Summary

While current detections are undeniably triggered by astronomical events, the evidence strongly suggests they are manifestations of rapid magnetic field variations from astronomical magnetized binaries (or precessing astronomical body). The global network has effectively functioned as an array of high-sensitivity magnetometers for sensing relativistic flux variations. Until a signal is confirmed in a magnetically isolated environment like KAGRA, the most rigorous interpretation is that LIGO and Virgo are detecting electromagnetic interactions. This necessitates a profound shift in our understanding of compact-object mergers and a reassessment of the role of magnetic fields in high-energy astrophysics.

These considerations suggest that magnetic interactions deserve renewed attention in astrophysical modeling. A comprehensive understanding of compact-object mergers, stellar evolution, and high-energy astrophysical phenomena may require a reassessment of the role of magnetic fields alongside gravitational and relativistic effects. Much remains to be explored.

ACKNOWLEDGEMENTS

No conflict of Interest

No funding

REFERENCES

1. Aasi, J., et al., (2012), The characterization of Virgo data and its impact on gravitational-wave searches. Classical and Quantum Gravity, 29 (15).
2. Abbott, B. P., et al. (LIGO Scientific Collaboration and Virgo Collaboration), (2016a), Observation of Gravitational Waves from a Binary Black Hole Merger, Phys. Rev. Lett., 116, 061102
3. Abbott, B. P., et al. (2016b), Characterization of transient noise in Advanced LIGO relevant to gravitational wave signal GW150914., Class. Quantum Grav. 33, 134001.
4. Abbott, B. P., et al. (2017), Gravitational waves and gamma-rays from a binary neutron star merger: GW170817 and GRB170817A, Astrophys. J. Lett., 848, L12
5. Abbott, B. P., et al. (2019), GWTC-1: A Gravitational-Wave Transient Catalog of Compact Binary Mergers Observed by LIGO and Virgo during the First and Second Observing Runs., Phys. Rev., X 9, 031040
6. Abbott B. P., et al (2020), A guide to LIGO–Virgo detector noise and extraction of transient gravitational-wave signals, Class. Quantum Grav., 37, 055002
7. Akutsu, T., Ando, M., Aoumi, M., et al. (2025). Identification of noise-associated glitches in KAGRA O3GK with hierarchical veto. Progress of Theoretical and Experimental Physics, 2025(8), 083F01.
8. Alexander, K. D., Berger, E., Fong, W., et al., (2017), The Electromagnetic Counterpart of the Binary

Neutron Star Merger LIGO/Virgo GW170817. VI. Radio Constraints on a Relativistic Jet and Predictions for Late-time Emission from the Kilonova Ejecta, The Astrophysical Journal Letters, 848, L21 (7pp).
9. Babcock, H. W. (1947). Zeeman Effect in Stellar Spectra. Astrophysical Journal, 105, p. 105.
10. Babcock, H. W. (1958). A Catalog of Magnetic Stars. Astrophysical Journal Supplement, 3, p. 141.
11. Biwer, C., Barker, D., Batch, et al. (2017). Validating gravitational-wave detections: The Advanced LIGO hardware injection system. Physical Review D, 95(6), 062002
12. Buchner, M., Höfler, K., Henne, B., Ney, V., & Ney, A. (2018), Tutorial: Basic principles, limits of detection, and pitfalls of highly sensitive SQUID magnetometry for nanomagnetism and spintronics. Journal of Applied Physics, 124(16), 161101.
13. Castañer, R., Medina, J. M., & Cuesta-Bolao, M. J. (2006). The magnetic dipole interaction as measured by spring dynamometers. American journal of physics, 74(6), 510-513.
14. Cirone, A., Chincarini, A., Neri, M., et al. (2018). Magnetic coupling to the advanced Virgo payloads and its impact on the low frequency sensitivity. Review of Scientific Instruments, 89 (11), 114501.
15. Coulter, D. A., Foley, R. J., Kilpatrick, C. D., et al. (2017). Swope Supernova Survey 2017a (SSS17a), the optical counterpart to a gravitational wave source. Science, 358 (6370), 1556-1558.
16. Cunha, M. S. (2006). Improved pulsating models of magnetic Ap stars—I. Exploring different magnetic field configurations. Monthly Notices of the Royal Astronomical Society, 365(1), 153-164.
17. Effler, A., Schofield, R. M. S., Frolov, V. V., et al. (2015). Environmental influences on the LIGO gravitational wave detectors during the 6th science run. Classical and Quantum Gravity, 32(3), 035017.
18. Hubrig, S., Järvinen, S. P., Korhonen, H., Ilyin, I., Schöller, M., et al. (2020a). Detection of weak magnetic fields in two HgMn stars. Monthly Notices of the Royal Astronomical Society: Letters, 495(1), L97-L101.
19. Hubrig, S., Schöller, M., Cikota, A., & Järvinen, S. P. (2020b). The search for magnetic fields in two Wolf–Rayet stars and the discovery of a variable magnetic field in WR 55. Monthly Notices of the Royal Astronomical Society: Letters, 499(1), L116-L120.
20. Kochukhov, O., (2015), Diagnostic of stellar magnetic fields with cumulative circular polarisation profiles, A&A, 580, A39. DOI: 10.1051/0004-6361/201526318
21. Kowalska-Leszczynska, I., et al. (2017) Globally coherent short duration magnetic field transients and their effect on ground based gravitational-wave detectors. Classical and Quantum Gravity, 34(7):074002, 4
22. Kun, E., Gabányi, K. É., Karouzos, M., Britzen, S., & Gergely, L. Á. (2014). A spinning supermassive black hole binary model consistent with VLBI observations of the S5 1928+ 738 jet. Monthly Notices of the Royal Astronomical Society, 445(2), 1370-1382.
23. Lundin, A., (2010), Magnetic Fields of Massive Stars, Department of Physics and Astronomy, Uppsala Universitet
24. Mahoney, A. W., & Abbott, J. J. (2014). Generating rotating magnetic fields with a single permanent magnet for propulsion of untethered magnetic devices in a lumen. IEEE Transactions on Robotics, 30 (2), 411-420.
25. Mahoney, A. W., Cowan, D. L., Miller, K. M., & Abbott, J. J., (2012) Control of Untethered Magnetically Actuated Tools using a Rotating Permanent Magnet in any Position, 2012. IEEE International Conference on Robotics and Automation. IEEE. p. 3375-3380
26. Margutti, R., Berger, E., Fong, W., et al. (2017), The Electromagnetic Counterpart of the Binary Neutron Star Merger LIGO/Virgo GW170817. V. Rising X-Ray Emission from an Off-axis Jet, The Astrophysical Journal Letters, 848:L20 (7pp),
27. Marklund, M., Brodin, G., & Dunsby, P. K. (2000). Radio wave emissions due to gravitational radiation. The Astrophysical Journal, 536(2), 875.
28. Mei, X., & Yu, P., (2016) Did LIGO Really Detect Gravitational Waves?—The Existence of Electromagnetic Interaction Made the Experiments of LIGO Invalid. Journal of Modern Physics, **7**, 1098-1104.
29. Michimura , Y., Shimoda, T., Miyamoto, T., et al., (2017), Mirror actuation design for the interferometer control of the KAGRA gravitational wave telescope, Classical and Quantum Gravity, 34, 225001
30. Nicholl, M., Berger, E., Kasen, D., et al. (2017). The electromagnetic counterpart of the binary neutron star merger LIGO/Virgo GW170817. III. Optical and UV spectra of a blue kilonova from fast polar ejecta. The Astrophysical Journal Letters, 848 (2), L18.

31. Sinha, M., & Mukhopadhyay, B., (2013). Instability of neutron star matter in high magnetic field: constraint on central magnetic field of magnetars, Nucl. Phys., A 898, 43-58.
32. Solomon, I., (1955). Relaxation processes in a system of two spins. Physical Review; 99(1):559-565
33. Szostek, R., Góralski, P., & Szostek, K., (2019) Gravitational Waves in Newton's Gravitation and Criticism of Gravitational Waves Resulting from the General Theory of Relativity (LIGO), Bulletin of the Karaganda University. Physics series, No 4 (96), 39-56, ISSN 2518-7198
34. Thrane, E., Christensen, N., & Schofield, R. M. (2013). Correlated magnetic noise in global networks of gravitational-wave detectors: observations and implications. Physical Review D, 87(12), 123009.
35. Ulianov, P. Y.; Mei, X.; & Yu., P. (2016) Was LIGO's Gravitational Wave Detection a False Alarm? Journal of Modern Physics, 7(14), 1845-1865
36. Voytsehovich, L.N., (2013), The theory of electromagnetic field motion. 6. Electron, Relativistic electromagnetism NO. 2, https://www.researchgate.net/publication/266558304
37. Walckiers, L., (2011) Magnetic measurement with coils and wires, https://arxiv.org/abs/1104.3784v1
38. Yung, K. W., Landecker, P. B., & Villani, D. D., (1998). An analytic solution for the force between two magnetic dipoles, Magnetic and Electrical Separation, Vol. 9, pp. 39-52
39. Ziaeepour, H., (2019), Binary Neutron Star (BNS) Merger: What We Learned from Relativistic Ejecta of GW/GRB 170817A, Physics, 1, 194–228